Efficient numerical simulation method for three dimensional resin flow in laminated preform during liquid composite molding processes

N. Chebil, M. Deléglise-Lagardère, C.H. Park

Efficient numerical simulation method for three dimensional resin flow in laminated preform during liquid composite molding processes

Naziha Chebil[1,2], Mylène Deléglise-Lagardère[1,2], Chung Hae Park[1,2*]

[1] IMT Lille Douai, Institut Mines-Télécom, Polymers and Composites Technology & Mechanical Engineering Department, 941 rue Charles Bourseul, 59508 Douai, France

[2] Université de Lille, 59000 Lille, France

* Corresponding author's e-mail: chung-hae.park@imt-lille-douai.fr ,

Telephone: +33 (0)3 2771 2187, Fax: +33 (0)3 2771 2981

Abstract

We propose an efficient simulation method of three-dimensional (3D) resin flow in laminated preform composed of multiple layers with different permeabilities at each layer. Because of the small thickness of each layer, a huge number of nodes are needed for 3D flow simulation if solid elements are adopted and full 3D simulation takes extremely long even by parallel computing. Instead of 3D solid elements, we propose multi-layered shell elements for 3D flow simulation with a short computing time. We describe the numerical formulation of multi-layered shell element method to consider the through-thickness flow as well as the planar flow. The accuracy and efficiency are evaluated by new dimensionless parameters defined in terms of preform permeability ratio and of the ratio of shell element size to the distance between the adjacent layers. Some simulation results are presented to demonstrate the advantages of the multi-layered shell element method for 3D flow simulation.

Keywords: C. Finite element analysis (FEA); C. Process simulation; E. Liquid composite molding; E. Resin flow

1. Introduction

Liquid composite molding (LCM) processes such as resin transfer molding (RTM) and vacuum assisted resin transfer molding (VARTM) processes are widely adopted to manufacture fiber reinforced polymer composites in many industrial sectors such as aeronautic, automobile and marine industries. In these manufacturing techniques, dry fiber reinforcement preplaced in a mold, a.k.a. preform, is impregnated by liquid resin. Hence, the analysis and optimization of the resin flow in a fiber preform is a critical step to minimize the process cycle time and improve the final part quality [1].

In general, the resin flow in a fiber preform is described by Darcy's law assuming the fiber preform as a porous medium [2]. In many cases, a fiber preform is composed of a number of different layers whose orientation and stacking sequence are decided to optimize the mechanical performance. Thus, the permeability tensor which is determined by the fiber arrangement in a fiber reinforcement, may be also different at each layer according to the different fiber orientation and fiber volume fraction. In the case of the VARTM process where a highly permeable distribution medium (DM) is mounted on top of the preform, the difference of permeability between the DM and the preform is very significant. Hence, the resin flow advances much faster in the DM than in the preform, resulting in a flow lead-lag effect (see Figure 1(a)) [3-6]. Through the flow lead-lag zone, the resin flow takes places from the DM to the preform in the thickness direction. Therefore, the through-thickness flow plays an important role in the mold filling process and the permeability in the thickness direction is a key parameter in the mold filling analysis.

Some analytical models have been developed to predict the flow front advancement in the VARTM process [3-5]. The analytical solution for the flow front advancing velocity in the DM and the preform with constant permeability, fiber volume fraction and thickness, was derived. These solutions are limited to two-dimensional (2D) cases where only the one longitudinal direction and the thickness direction are considered. Moreover, they are applicable only to a fully-developed flow where the flow front advancing velocity is the same at the DM and at the preform (see the flow pattern between t_0 and t_f in Figure 3(a), $u_1 = u_2$) [6]. Therefore, a three-dimensional (3D) numerical simulation is required for more general cases with a complex geometry and non-uniform properties [1, 7-8].

With respect to the numerical simulation of 3D resin flow, 3D solid elements such as tetrahedral or brick elements can be considered [1, 7-8]. To guarantee the good computational accuracy, the aspect ratio of elements, i.e. the ratio of the greatest dimension to the smallest dimension of an element, should be close to one. Due to the small thickness of a single ply, for example order of 100 μm in the cases of a preform fabricated by automated dry fiber placement (ADFP), small elements whose size is not bigger than the single ply thickness should be used. This constraint on the element size can lead to a significant increase of the mesh size for 3D simulation. For example, about 300 million nodes would be needed in 3D simulation even for a small part whose dimensions are 300×300×3 mm^3 if the size of element is 0.1 mm. With such a huge number of nodes, 3D transient flow simulations are extremely heavy even by parallel

computing [9]. Hence, the numerical simulation with 3D solid elements is no more practical for industrial developments.

Many composite structures have a shell-like body whose planar dimensions are much greater than the thickness. Hence, shell elements are commonly used in the numerical simulation of mold filling process for such structures. In such a simulation scheme, through-thickness flow is ignored and arithmetic gapwise-averaged permeability tensor is adopted to model the resin flow in the planar directions (compare Figures 1(b) and 1(c)) [10-11].

$$K_{ij,ave} = \left(\sum_{k=1}^{N_{layer}} K_{ij,k} \times h_k\right) / \left(\sum_{k=1}^{N_{layer}} h_k\right) \qquad i, j = 1, 2 \qquad (1)$$

where $K_{ij,ave}$ is the gapwise-averaged permeability tensor, N_{layer} is the number of layers, $K_{ij,k}$ is the permeability tensor of the kth layer and h_k is the thickness of the kth layer. It is well-known that this model is no more valid if the ratio of permeability between adjacent layers is great, for example DM and preform whose permeability ratio is significant such as 100 or 1000 [11]. Moreover, layer stacking sequence cannot be considered in this model whereas it can have a great influence on the mold filling process [12]. The most crucial is the ignorance of the through-thickness flow which plays a key role in many LCM processes such as VARTM process and Liquid Resin Infusion (LRI) process. To take into account the through-thickness flow between the adjacent layers, a couple of analytical models were proposed to obtain effective average permeability tensors [13-14]. These models were based on the assumption that the pressure distribution in each layer was linear. At the partially saturated zone where the flow takes place in the thickness direction (see Figure 1(a)), however, the pressure distribution is no more linear. Moreover, the layer stacking sequence such as the position of DM (e.g. on top of a preform or in the middle of a preform) cannot be considered either, even if it has a big influence on the mold filling process [12].

For 3D flow simulation with a reduced computational cost, Kang and Lee proposed a dual scale flow simulation [15]. In this approach, a two-dimensional (2D) macroscopic flow was simulated by shell elements with the gapwise-averaged permeability tensor of DM and preform stack. Then, the pressure values in a local zone obtained by the 2D simulation were used as the boundary conditions for the 3D flow simulation with 3D tetrahedral elements at the local zone. Even if the 3D flow can be simulated at a local zone, this dual scale simulation approach may be misleading because the pressure values used as the boundary conditions should be obtained by a 2D simulation using the gapwise-averaged permeability

model which is not valid due to a big difference of permeability between DM and preform. To lessen the computational burden for 3D flow simulation of VARTM process, a model for an equivalent permeability of DM was proposed [16-17]. Dong et al. developed a model to virtually increase the thickness of DM with equivalent permeability and fiber volume fraction while keeping the same flow kinematics [16-17]. By this approach, the thickness of DM in the numerical simulation can be increased by several times from the real value of DM and bigger elements can be adopted in the flow simulation. If a preform is composed of a number of layers whose permeability is different for each layer with a small thickness, however, this approach cannot be applied and small elements are still required to model the preform. Thus, a heavy computational burden is inevitable in numerical simulations using 3D solid elements. Moreover, this method cannot be extended to 3D solid elements if the permeabilities in x direction and in y direction are different. To avoid the use of 3D solid elements, Sun and Lee proposed to use two shell element mesh systems to sequentially simulate the resin flows in the DM and in the preform [18]. They adopted a shell element mesh for the DM and another for the preform. The 2D flow in the DM was simulated to obtain the pressure field in the DM without taking into account the flow in the preform. Subsequently, the flow in the preform was computed by introducing the leakage flow which came from the DM to the preform in the thickness direction. It should be kept in mind that the pressure values in the DM were used as the input data for the simulation of the flow in the preform. In fact, the through-thickness flow has an adverse influence on the flow front advancement in the DM whereas it accelerates the flow in the preform. Hence, this adverse effect of the through-thickness flow on the DM could not be considered in their approach and the flow front advancement in the DM might be overestimated. Indeed, the flows in the DM and in the preform are strongly coupled via the through-thickness flow and all the flow fields should be simultaneously solved.

We propose a new multi-layered shell element method to simulate 3D resin flow by Darcy's law with a reduced computational cost. An advantage of shell elements is that the element size can be much greater than the thickness of a structure. However, the through-thickness flow cannot be taken into account by classic shell elements. Hence, we propose a new formulation of multi-layered shell elements to consider both the through-thickness flow and the planar flow. Then, we examine the convergence criterion according to the size of shell elements and the ratio of permeability between different directions. In the

subsequent sections, we present the mesh generation for a laminated preform, the numerical formulation, the assessment of the accuracy and of the computational cost, and some simulation examples.

2. Numerical method

2.1 Mesh generation

In a multi-layered shell element mesh, each ply in a laminated preform is discretized by shell elements (see Figure 2). To begin with, a layer in the center of the preform is selected and modeled by a single layer of triangular shell elements whose position is located on the mid-plane of the selected layer. Then, a normal vector is defined at each node in the shell elements mesh. A node is created on the adjacent layer by shifting the coordinates of the current node in the direction of the normal vector by a distance which is the sum of the half thickness of the current layer and of the half thickness of the adjacent layer.

$$\vec{x}_{n,k+1} = \vec{x}_{n,k} + 0.5\left(h_{n,k} + h_{n,k+1}\right)\vec{n}_{v,n} \tag{2}$$

$$\vec{x}_{n,k-1} = \vec{x}_{n,k} - 0.5\left(h_{n,k} + h_{n,k-1}\right)\vec{n}_{v,n} \tag{3}$$

where, for the node n in the kth layer, $\vec{x}_{n,k}$ is the coordinates of the node, $\vec{n}_{v,n}$ is the normal vector of the node and $h_{n,k}$ is the thickness of the layer. The subscripts n and k represents the node number and the layer number, respectively. This procedure is repeated until all the nodes are created on all the layers. It should be noted that the number of layers can be varied according to the position. For each element, any values of permeability tensors, thickness and fiber volume fraction can be assigned. For the finite element calculation, the information of the corresponding nodes at the adjacent layers as well as the information of the nodes sharing the same elements at the same layer should be recorded.

2.2 Numerical formulation

We assume an isothermal flow of incompressible fluid in a laminated preform. The mass conservation equation can be expressed by the following relation.

$$\frac{\partial u}{\partial x} + \frac{\partial v}{\partial y} + \frac{\partial w}{\partial z} = 0 \tag{4}$$

where u, v and w are the velocity components in the x, y and z coordinates, respectively. If we represent the velocity components with pressure gradient by applying Darcy's law, we can obtain the following relation.

$$\nabla_{x,y} \cdot \left(-\frac{K_{ij}}{\mu}\nabla_{x,y}P\right)_{i,j=x,y} - \frac{\partial}{\partial z}\left(\frac{K_z}{\mu}\frac{\partial P}{\partial z}\right) = 0 \tag{5}$$

where P is the resin pressure, μ is the resin viscosity, K_{ij} is the permeability tensor in the x-y plane and K_z is the permeability in the thickness direction.

Then, each triangular shell element is divided into three sub-elements (see Figure 3(a)) and the governing equation is integrated over control volume to obtain a weak formulation.

$$\int_{CV} \nabla_{x,y} \cdot \left(-\frac{K_{ij}}{\mu} \nabla_{x,y} P \right)_{i,j=x,y} dV_e - \int_{CV} \frac{\partial}{\partial z} \left(\frac{K_z}{\mu} \frac{\partial P}{\partial z} \right) dV_e = 0 \tag{6}$$

where CV represents the control volume which is the product of the control surface and the thickness.

The mass flux which is represented by the terms in the left hand side of Equation 6 can be treated by control volume finite element method (CVFEM) whose numerical formulation of the governing equation and definition of control volume are presented in Kang et al. [19]. By applying Green theorem and a linear polynomial shape function for pressure field, the first term can be converted into a linear integration for each node in the element (for example, consider the node 1 in Figure 3).

$$\int_{CV} \nabla_{x,y} \cdot \left(-\frac{K_{ij}}{\mu} \nabla_{x,y} P \right)_{i,j=x,y} dV_e = \int_{CS} \nabla_{x,y} \cdot \left(-\frac{K_{ij}}{\mu} \nabla_{x,y} P \right)_{i,j=x,y} h_e dA_e = \int_c^a -\frac{K_{ij}}{\mu} \nabla_{x,y} P \cdot \vec{n}_e \cdot h_e dl \tag{7}$$

where CS denotes the control surface of the sub-element related to the node. h_e is the thickness of the element and A_e is the surface area of the corresponding sub-element. $\vec{n}_e$ is the unit normal vector which gets across from the current node (i.e. node 1) to the other nodes (i.e. node 2 or node 3) in the same element.

We need a new method to deal with the second term in Equation 6 because the linear shape function used in the triangular shell elements cannot represent the pressure distribution in the thickness direction. For each node in the element, the corresponding nodes in the adjacent layers are identified (see Figure 3(b)). Then, the pressure gradient in the thickness direction is expressed by a finite difference scheme.

$$\left.\frac{\partial P}{\partial z}\right|_{up1} = \frac{P_{up1} - P_1}{\frac{h_{up1} + h_1}{2}} \tag{8}$$

$$\left.\frac{\partial P}{\partial z}\right|_{dw1} = \frac{P_1 - P_{dw1}}{\frac{h_1 + h_{dw1}}{2}} \tag{9}$$

where the upper node is denoted as the subscript, "$up1$" and the bottom node as "$dw1$" for the node 1 in Figure 3(b). It should be kept in mind that the adjacent layers may have different permeabilities from

those of the current layer. Hence, the average permeability in the thickness direction across the adjacent layers is obtained by the following relation.

$$K_{z,m} = (h_m + h_1) \Big/ \left(\frac{h_m}{K_{z,m}} + \frac{h_1}{K_{z,1}} \right), \quad m = up1, dw1 \tag{10}$$

The term with the second derivative of pressure is also obtained by a finite difference scheme.

$$\frac{\partial}{\partial z}\left(\frac{K_z}{\mu}\frac{\partial P}{\partial z}\right)\Big|_1 = \frac{2}{h_{up1}+2h_1+h_{dw1}}\left(K_{z,up1}\frac{\partial P}{\partial z}\Big|_{up1} - K_{z,dw1}\frac{\partial P}{\partial z}\Big|_{dw1}\right) \tag{11}$$

The terms involving either the upper node or the bottom node can be ignored if the corresponding node is absent, for example in the case of the first top layer or the last bottom layer.

Subsequently, these terms are multiplied by the corresponding control volume of a sub-element (i.e. node 1 in Figure 3) at the current layer, which is the product of the thickness and the surface area of the sub-element associated with node 1, to obtain the second term in Equation 6.

$$\int_{CV}\frac{\partial}{\partial z}\left(\frac{K_z}{\mu}\frac{\partial P}{\partial z}\right)dV_e = \frac{2}{h_{up1}+2h_1+h_{dw1}}\left(\frac{K_{z,up1}}{\mu}\frac{P_{up1}-P_1}{\frac{h_{up1}+h_1}{2}} - \frac{K_{z,dw1}}{\mu}\frac{P_1-P_{dw1}}{\frac{h_1+h_{dw1}}{2}}\right)h_1 CS_1 \tag{12}$$

To sum up, the first term of Equation 6 can be transformed into an algebraic equation associated with three nodal pressure values, viz. $C_1P_1+C_2P_2+C_3P_3$ whereas the second term of Equation 6 is represented with three nodal values, viz. $C_{11}P_1+C_{up1}P_{up1}+C_{dw1}P_{dw1}$. Consequently, for each node in an element, we can obtain an element matrix associated with five nodal pressure values. This elementary matrix is obtained for each node per element and is assembled in the global matrix as shown in the following relation.

$$\begin{bmatrix} C_{up1} & & & & \\ & C_1 + C_{11} & & & \\ & & C_2 & & \\ & & & C_3 & \\ & & & & C_{dw1} \end{bmatrix} \begin{Bmatrix} P_{up1} \\ P_1 \\ P_2 \\ P_3 \\ P_{dw1} \end{Bmatrix} = \begin{Bmatrix} d_{upl} \\ d_1 \\ d_2 \\ d_3 \\ d_{dw1} \end{Bmatrix} \tag{13}$$

where d_n (n=1, 2, 3, $up1$, $dw1$) is the force vector which is represented in terms of boundary conditions such as flow volume rate or injection pressure at the resin inlets or the air vents. By solving a set of algebraic equation represented as Equation (13), we can obtain pressure field from which the velocity field can be calculated by Darcy's law.

To deal with the flow front advancement, the volume of fluid (VOF) method is employed [20]. The increment of fill factor can be computed by considering the mass flux into the current control volume both within the same layer and across the adjacent layers.

$$\frac{df_n}{dt} = \frac{Q_{n,xy} + Q_{n,z}}{CV_n} \tag{14}$$

where f_n is the fill factor of the node n and CV_n is the control volume of the node n. $Q_{n,xy}$ and $Q_{n,z}$ are the volume flow rates in the planar direction and in the thickness direction, respectively, which can be obtained as the product of the flow velocity in the corresponding direction and the cross-section of the control volume. The velocity component in the thickness direction is calculated from the pressure gradient calculated by finite difference scheme as described by Equations 8 and 9 and from the average permeability in the thickness direction obtained by Equation 10. Then, the through-thickness flow velocity component obtained by Darcy's law is multiplied by the control surface to calculate the mass flux in the thickness direction as shown in the following relation.

$$Q_{n,z} = -CS_n \left(\frac{K_{z,up1}}{\mu} \frac{\partial P}{\partial z}\bigg|_{up1} - \frac{K_{z,dw1}}{\mu} \frac{\partial P}{\partial z}\bigg|_{dw1} \right) \tag{15}$$

where CS_n is the control surface associated with the nth node. Once the increment of fill factor is obtained at each node, the time increment to completely fill the control volume is computed at each node. Then, the minimum time increment among them is selected. The fill factor at each node is updated by adding to the current fill factor the product of the minimum time increment and the increment of fill factor at the corresponding node.

3. Verification of the numerical method: accuracy and efficiency

3.1 Presentation of verification methods

In this section, we verify the accuracy and the computational cost of the multi-layered shell element method. As a benchmark test, we considered resin impregnation into a stack of a DM and a preform with a rectangular prism shape (see Figure 4(a)). The preform was composed of four identical layers with a same thickness of 0.2 mm. The permeability values of DM and of preform for the flow simulations are listed in Table 1. The injection pressure applied along the top edge line of DM was a constant value of 1 bar and the vent pressure of 0 bar was applied along the bottom edge line of preform. The resin viscosity was 0.1 Pa·s.

It is a common practice to compare simulation results with experimental results to assess the accuracy of a numerical method. On the other hand, there are still many arguments about the permeability measurement whose reliability is the most crucial for the accurate numerical simulation [21-22]. Instead, we performed flow simulations for given permeability tensors, using a conventional numerical method whose reliability has been already proven and widely accepted. Then, their corresponding results were regarded as the exact solution. Because full 3D simulations with 3D solid elements are very heavy, we performed numerical simulations of 2D flow in the *x*-*z* plane while ignoring the flow in *y* direction and the corresponding results were considered as the exact solution. To assess the accuracy, the flow pattern on the *x*-*z* plane obtained by 2D simulation was compared with that on the *x*-*z* plane obtained by 3D flow simulation using the multi-layered shell element method. To evaluate the computational efficiency, however, the computational time of 3D flow simulation using the multi-layered shell element method was compared with that of 3D flow simulation using the tetrahedral element method [7].

3.2 Accuracy

Given the properties and conditions defined in Table 1 and in Figure 4(a), flow simulations were performed both by 2D shell elements in the *x*-*z* plane and by multi-layered shell elements in 3D space. The dimensions of multi-layered shell element were defined as shown in Figure 4(b). The element dimensions in the planar directions, viz. *dx* and *dy* in Figure 4(b) were defined as the lengths of triangular shell element in the *x* and *y* directions, respectively whereas *dz* was the distance between the adjacent layers or the thickness of a single layer if all the layers had a same thickness. In the first calculation, the dimensions of multi-layered shell elements, i.e. *dx* and *dy*, were set to be equal to the thickness of a single layer, i.e. *dz*, so that the mesh resolution could be the same both in the planar directions and in the thickness direction. For the 2D simulation in the *x*-*z* plane, the element dimensions in *x* and *z* directions, i.e. *dx* and *dz*, were set to be identical (see the right figures in Figure 4(b)). The results obtained by the two methods are compared in Figure 5. For the simulation by the multi-layered shell elements, the results are represented only at the *x*-*z* plane for the sake of clarity in comparison, even if a full 3D simulation was performed. We can see that the simulation results by both methods are in a good agreement with respect to the flow front advancement and the pressure distribution. A particular characteristic feature of the mold filling in the VARTM process is a constant length of flow lead-lag between the DM and the preform (see $t_o < t < t_f$ in Figure 1(a)) [6]. In the beginning of the mold filling process, the flow in the DM advances

faster than in the preform and the length of the flow lead-lag between these two layers gradually grows (see $0 < t < t_o$ in Figure 1(a)). Once the flow is fully-developed (see $t_o < t < t_f$ in Figure 1(a)), however, the flow in the DM and that in the preform are equilibrated through the flow in the thickness direction and the two flow fronts at the DM and the preform advance with a same velocity while maintaining a constant lead-lag length. We can see that this constant lead-lag length is properly represented in the simulation result by multi-layered shell elements (see the vertical arrows in Figure 5(b)). Another characteristic feature is non-linear pressure distribution in the partially saturated zone. The pressure distribution is linear and almost identical both at the DM and at the preform in the fully-saturated zone where there is no through-thickness flow between the adjacent layers (see Figures 5(c) and 5(d)). Near the flow front where the flow in the thickness direction takes place, the pressure distribution is non-linear which shows the limit of the gapwise-averaged permeability model where the linear pressure distribution is assumed [10, 11, 13, 14]. Moreover, the signs of the pressure profile curvature in the DM and in the preform are opposite (see the red circle and the red box inside the graph in Figure 5(d)). This transition from linear to non-linear pressure profile is also properly represented in the result of the multi-layered shell element simulation.

An important advantage of the multi-layered shell elements is that big shell elements whose size is much greater than the thickness can be employed. For the same condition used in the previous simulation (i.e. Table 1 and Figure 4(a)), another 3D flow simulation using multi-layered shell elements was performed with bigger elements whose planar dimensions were 50 times greater than the thickness of a single ply (i.e. $dx = dy = 50dz$). For the 2D simulation, the same small elements (i.e. $dx = dz = 0.2$ mm) were used to ensure the accuracy. We could obtain the same results as shown in Figure 5, by the multi-layered shell elements even if the shell element dimensions were much bigger than the single ply thickness.

We assessed the accuracy of the multi-layered shell elements method for different cases of permeability ratio and of element size. We selected three parameters which might affect the accuracy of the multi-layered shell elements method, viz. the ratio of the shell element dimension in x direction to the distance between the adjacent layers or the thickness of a single layer (i.e. dx/dz), the ratio of the preform permeability in x direction to the preform permeability in z direction (i.e. K_{xp}/K_{zp}), and the ratio of the DM permeability in x direction to the preform permeability in x direction (i.e. K_{xd}/K_{xp}). For these three parameters, a total 80 cases were tested (see Table 2; 10 cases for dx/dz × 4 cases for K_{xp}/K_{zp} × 2 cases for

K_{xd}/K_{xp}). To quantitatively evaluate the accuracy, an error function was defined in terms of the flow front arrival time at each node.

$$Error = \frac{1}{N_n}\sum_{n=1}^{N_n}\left(\frac{t_{n,ML} - t_{n,2D}}{t_{n,2D}}\right)^2 \tag{16}$$

where *Error* is the error function, N_n is the total number of nodes on the x-z plane in the multi-layered shell element mesh, $t_{n,2D}$ is the flow front arrival time at the nth node obtained by the 2D simulation in the x-z plane and $t_{n,ML}$ is the flow front arrival time at the nth node on the x-z plane obtained by the 3D simulation using the multi-layered shell elements. It should be kept in mind that small elements (i.e. dx = dz = 0.2 mm) were employed in the 2D simulation on the x-z plane to obtain accurate solutions which were considered as the exact values.

We show some results of the case studies in Figure 6. We can see that the error is increased as the element size (i.e. dx/dz) is increased (see Figure 6(a)). The error is decreased as the ratio of the longitudinal permeability to the through-thickness permeability of preform (i.e. K_{xp}/K_{zp}) is increased, because the relative influence of the flow in the thickness flow to the flow in the planar direction is decreased (see Figure 6(b)). For example, if K_{zp} is zero (i.e. $K_{xp}/K_{zp} = \infty$), there is no through-thickness flow between the adjacent layers and the multi-layered shell element simulation becomes the independent 2D shell element simulation on each x-y plane at different z coordinates. With respect to the ratio of the longitudinal permeability of DM to the longitudinal permeability of preform (i.e. K_{xd}/K_{xp}), there is no significant correlation (see Figure 6(c)). We can consider two following extreme cases to interpret this result. If the longitudinal permeability of DM is much bigger than the longitudinal permeability of preform (i.e. $K_{xd} >> K_{xp}$), the flow advances fast in the DM and most of the flow takes place in the unidirectional direction along the thickness. On the contrary, the flows in the DM and in the preform advances in parallel and there will be no through-thickness flow if the longitudinal permeability of DM is the same as the longitudinal permeability of preform (i.e. $K_{xd} = K_{xp}$). In both cases, there is no coupling between the planar flow and the transverse flow. Therefore, we can conclude that the influence from the ratio of the longitudinal permeability of DM to the longitudinal permeability of preform is insignificant.

From the mass conservation equation coupled with Darcy's law, we can verify this speculation. For the sake of simplicity, the flow in y direction is not taken into account. By introducing dimensionless variables, we can derive the following dimensionless equation.

$$\frac{\partial^2 P^*}{\partial x^{*2}} = -\frac{K_{zp}}{K_{xp}}\left(\frac{dx}{dz}\right)^2 \frac{\partial^2 P^*}{\partial z^{*2}} = -\varepsilon \frac{\partial^2 P^*}{\partial z^{*2}} \tag{17}$$

where P^* is the dimensionless pressure, x^* is the dimensionless x coordinate ($x^* = x/dx$) and z^* is the dimensionless z coordinate ($z^* = z/dz$). ε is the dimensionless parameter defined in terms of the element size ratio and the ratio of the through-thickness to longitudinal permeabilities of preform.

$$\varepsilon = \frac{K_{zp}}{K_{xp}}\left(\frac{dx}{dz}\right)^2 \tag{18}$$

As ε is increased in the right hand side of Equation (17), the mass flux in the thickness direction becomes more important and the error in the multi-layered shell element method is increased.

Subsequently, we plotted all the results in a same graph by representing the error against this dimensionless parameter, ε. As shown in Figure 7, we could obtain a master curve expressed in an exponential equation.

$$Error = 0.0018 \times \varepsilon^{0.3578} = 0.0018 \times \left[\frac{K_{zp}}{K_{xp}}\left(\frac{dx}{dz}\right)^2\right]^{0.3578} \tag{19}$$

Given the permeability values and the thickness of a single layer in the preform, this master curve can provide practical information to decide the mesh resolution for 3D flow simulation using multi-layered shell elements. For example, we can consider a preform with a ratio of the longitudinal to the transverse permeabilities (i.e. K_{zp}/K_{xp}) of 10^{-3} and the thickness of a single layer (i.e. dz) of 0.2 mm. In this case, we can assume an approximate error about 2% if we adopt big elements with a size of 200 mm (i.e. $dx/dz = 10^3$). This error function can provide an approximate estimation of the order of magnitude of error and very useful information to determine the element size before real computation.

3.3 Numerical efficiency

The multi-layered shell element method can reduce the computational time compared with 3D solid element methods because shell elements can have a greater size than the thickness of a single layer and the number of nodes can be significantly reduced. We investigated the numerical efficiency in a quantitative manner by comparing the computational time between the 3D solid element method and the multi-layered shell element method. We considered the mold filling process in a rectangular prism preform covered with a DM which was a similar one as shown in Figure 4. For the evaluation of the numerical efficiency, however, the total number of layers in the stack of preform and DM was varied. For

each case, 3D flow simulations using the multi-layered shell elements and 3D flow simulation using the tetrahedral elements were performed [7]. In both element types, the same element size was adopted (i.e. $dx = dy = dz = 0.2$ mm). All the parameters listed in Table 1 were adopted in the simulations except the preform thickness which was proportional to the number of layers.

As a measure of the numerical efficiency, we defined the coefficient of efficiency, *CE*, as the ratio of the computational time for the 3D simulation using the multi-layered shell elements, $t_{c,ML}$, to that using the tetrahedral elements, $t_{c,3D}$.

$$CE = \frac{t_{c,ML}}{t_{c,3D}} \tag{20}$$

In general, the computational time of transient flow simulation is roughly proportional to the square of the number of nodes. If we adopt the same mesh resolution and assume that the number of the nodes in the *x*-*y* plane is the same for the 3D tetrahedral element mesh and the multi-layered shell element mesh, the total number of nodes in the 3D tetrahedral element mesh is proportional to the number of layers plus one and the total number of nodes in the multi-layered shell element mesh is proportional to the number of layers. From the results of the computations, we could obtain a following relation between the coefficient of efficiency and the number of layers (see Figure 8).

$$CE\_iso = 0.1 \times \left(\frac{N_{layer}}{(N_{layer}+1)} \right)^2 \tag{21}$$

where *CE_iso* is the coefficient of efficiency when the same mesh resolution is applied both for the 3D solid element mesh and for the multi-layered shell element mesh, and N_{layer} is the total number of layers in the preform. Because the computational time is approximately proportional to the square of number of nodes, we can express the coefficient of efficiency for multi-layered shell elements (*CE*) with a bigger size than the single ply thickness, in the following relation.

$$CE = 0.1 \times \left(\frac{N_{layer}}{(N_{layer}+1)} \right)^2 \times \left(\frac{dx}{dz} \right)^2 \times \left(\frac{dy}{dz} \right)^2 \tag{22}$$

If we consider again the same example introduced in the end of the previous section 3.2, we can expect only 10^{-7} of the computational time required for 3D solid element mesh, when employing big multi-layered shell elements (e.g. $dx = dy = 1000dz$) with a marginal error less than 5%. This implies that 3D flow simulation for a huge structure laminated with thin plies, for example off-shore wind turbine blade,

can be done by multi-layered shell elements with a single ordinary PC in a few hours, which would require an excessive computational resource if 3D solid element mesh is employed.

4. Simulation examples

We present the 3D flow simulation results of three examples of laminated preform, viz. quasi-isotropic lay-up of unidirectional plies, VARTM of a boat hull and VARTM of hat-shaped stiffeners. It should be emphasized that a huge number of nodes (e.g. at least order of 100 million nodes) are required for 3D solid element mesh for all these cases and the transient 3D flow simulation would take extremely long or even practically impossible.

4.1. Quasi-isotropic lay-up of unidirectional plies

To maximize the in-plane stiffness and strength, thin unidirectional plies are stacked in quasi-isotropic lay-up, to obtain non-crimp fabrics or ADFP preform [23]. Because the fiber orientation in each ply is different, it is desirable to perform a full 3D flow simulation for such preforms. Due to the very small thickness of each ply and the big computational cost required for the 3D simulation with solid elements, however, 2D flow simulation is generally conducted while ignoring the through-thickness flow and adopting the homogenized permeability tensor of a laminated preform. Nevertheless, the assumption of plug flow (see Figure 1(c)) may not be valid if the through-thickness permeability is low. We investigate the influence of the through-thickness permeability on the 3D flow characteristics in quasi-isotropic lay-up of UD plies.

We considered the mold filling process of a rectangular preform whose dimensions were 300×300×1.6 mm^3. The preform was composed of eight layers which were numbered from top to bottom. The layer stacking sequence was $[0/90/-45/45]_s$. The resin was injected at a single point gate located at the center of the top layer (i.e. Layer 1) and the injection pressure was a constant value of 1 bar. The resin viscosity was 0.1 Pa·s and the thickness of single ply was 0.2 mm. Because each ply has a highly anisotropic permeability tensor (i.e. $K_1 = 1.2075\times10^{-12}$ m^2, $K_2 = 2.6175\times10^{-13}$ m^2) the resin flow pattern in a single ply without the other adjacent plies exhibits an ellipsoidal flow front which is highly elongated along the fiber direction.

We performed 3D flow simulations using multi-layered shell elements whose element size ratio was 50 (i.e. $dx = dy = 50dz = 10$ mm). A simulation example is presented in a video (see Video 1 in the appendix). To clearly show the 3D flow pattern, the z coordinate was magnified by 100 times. By dint of the big size

of elements, the total number of nodes was only 7688 and the computational time was 1 hour for 3D flow simulation (by Intel Core I7-3770, CPU at 3.40 GHz 4 Core). We can see that the 3D flow pattern is well represented by the multi-layered shell element method. In particular, the flow front shape in the bottom layers becomes circular whereas the flow front shape in the top layer is ellipsoidal. We can assume that the effect of through-thickness flow becomes significant as the flow front advances in the thickness direction and the anisotropic flow pattern in the *x*-*y* plane at different layers is averaged out to lead to a circular flow front. Thus, this flow pattern may depend on the through-thickness permeability.

We compare the flow patterns for two different ratios of the permeability in the planar direction to that in the thickness direction (i.e. K_2/K_3 = 100 or 1000). Before running the simulations, we estimated an approximate error according to Equation 19. For both ratios (K_2/K_3 = 100 or 1000), the approximate errors were smaller than 1 % (i.e. 3.3×10^{-3} for K_2/K_3 = 100 and 1.45×10^{-3} for K_2/K_3 = 1000). The flow patterns in the *x*-*y* plane at each layer are shown in Figures 9 and 10. If the permeability in the thickness direction is not low enough (i.e. K_2/K_3 = 100), the flow patterns in all the layers exhibit almost the same contour with a circular flow front (see Figure 9). Hence, the through-thickness flow between the adjacent layers compensates the difference of planar flow between the layers and the flow front advances with the same velocity at all the layers (as shown in Figure 1(c)). Conversely, if the through-thickness permeability is sufficiently low (i.e. K_2/K_3 = 1000), the flow in the thickness flow is insignificant and the planar flow in the upper layers exhibits its own anisotropic flow pattern according to the ply orientation (see Layer 1 in Figure 10). Nevertheless, this anisotropy of flow pattern is lessened as the flow advances further in the thickness direction and the flow front shape becomes circular at the bottom layers (see Layer 8 in Figure 10). Commercial grades of UD carbon tapes for ADFP process have the ratio of planar to through-thickness permeabilities of about 100 to 1000 [23]. Thus, for the preforms made of some grades of carbon UD tapes, the assumption of plug flow and the gapwise-averaged permeability model would not hold good and 3D flow simulation with multi-layered shell elements would be very useful.

4.2 VARTM of a boat hull

We considered mold filling simulation for the manufacturing of a boat hull by the VARTM process. The preform was composed of three layers of fiber reinforcement with anisotropic permeabilities and was covered with a DM. The material properties are presented in Table 3. The resin with a viscosity of 0.1 Pa·s was injected at the center of the DM under a constant pressure of 1 bar (see Figure 11(a)).

The results of mold filling simulation are shown at each layer in Figure 11(b). We can verify a delay of flow front advancement at the bottom layer of preform whereas the flow front advances fast at the DM. To clearly see the difference between the conventional 2D shell element method coupled with the gapwise-averaged permeability model and the 3D multi-layered shell element method with different permeabilities at each layer, we defined the gapwise-averaged fill factor, f_{ave}.

$$f_{ave} = \frac{\sum_{k=1}^{N_{layer}} h_k \times f_k}{\sum_{k=1}^{N_{layer}} h_k} \tag{23}$$

The results of mold filling simulation are shown in terms of the gapwise-averaged fill factor in Figure 11(c). We can see that, in the simulation result by the conventional 2D shell element approach, there is a sharp transition of the gapwise-averaged fill factor which changes from zero to one at the flow front, because plug flow was assumed and no through-thickness flow was considered (see the left figures in Figure 11(c)). Conversely, in the simulation result by the multi-layered shell element approach, we can see a relatively wide partially saturated zone (i.e. $0 < f_{ave} < 1$) which corresponds to the flow lead-lag length between the top and bottom layers (see the right figures in Figure 11c)). In fact, the estimation of this flow lead-lag length between the DM and the preform is a key issue in the VARTM optimization to avoid air entrapment [5, 15]. It should be also noted that the length of this partially saturated zone depends on the permeabilities of preform and of DM in the multi-layered shell element simulation whereas it does not depend on the material properties but on the element size in the conventional 2D shell element simulation coupled with the gapwise-averaged permeability model.

4.3 VARTM of hat-shaped stiffeners

A common composite structure adopted in the aircraft design is a hat-shaped stiffener to enhance the flexural stiffness and reduce the structural weight [24]. In this structure, the resin flow is divided into two paths, viz, the one along the top section of the hat-shaped stiffener and the other along the bottom section. Hence, the resin flow lengths in these sections are different and there is a risk of air entrapment at the junction of the two flow paths. To accelerate the resin flow in the long flow path on the top section, a DM is often mounted on top of the preform. In real practice, it is crucial to design the distribution medium, in particular, by adjusting its length. We compare the resin flow patterns in two cases of DM length, obtained by the multi-layered shell element method. The geometry and dimensions of the hat-shaped stiffener are shown in Figures 12(a) and 12(b). The two configurations of DM considered for the

numerical simulation of resin flow are presented in Figure 12(c) and the numerical mesh systems for multi-layered shell element simulation are illustrated in Figure 12(d). The injection pressure was a constant value of 1 bar and the resin viscosity was 0.1 Pa·s. The properties of DM and of preform used for flow simulation are listed in Table 4. The preform was composed of eight layers whose thickness was 0.2 mm for each layer. Four layers were included in the hat-shaped section and four layers were included in the bottom section.

The results of flow simulation are shown in Figure 13. The computation times were 2399 s for the case 1 and 2046 s for the case 2, respectively (with dx/dz = 50, Intel Core™ I7-3770 CPU 3.40 GHz 4 Core). In Figures 13(a) and 13(b), the flow front arrival time is shown only for the top layer and the bottom layer of the preform. In particular, we can compare two points, A and B in Figure 13(a), which are at the same position on the x-y plane but at the different positions along z direction. Because the point A is near the DM, the flow front arrival time is shorter than for the point B which is far from the injection gate. If the conventional 2D shell element method with the gapwise-averaged permeability model is applied, the flow front arrival time should be the same for these two points. Then, we can compare the points B and C in Figure 13(a). Even if the point C is located in the downstream, the flow front arrives at the point C before it arrives at the point B located in the upstream. The flat section where the point B is located, has a greater number of layers, i.e. eight. Hence, it takes longer for the resin to flow through the whole thickness to the point B, than to flow along the planar direction and to reach the point C in the downstream. This phenomenon that the flow front arrives in the downstream faster than in the upstream cannot be represented by the conventional 2D shell elements and the gapwise-averaged permeability model.

We can also see that the short DM configuration leads to smaller air entrapment at the bottom section than the long DM configuration as shown in Figures 13(a) and 13(b). This result can be explained by the flow front advancement pattern. In Figure 13(a), three flow front positions (see the red contours) are observed at the bottom layer, viz. the first one of the flow advancing through the bottom section, the second one of the flow through the top section which turns back at the junction of the top and bottom sections, and the third one of the flow which comes from the top section and continues in the same direction after the junction. We can see that the difference between these flow front positions is relatively large and the corresponding air entrapment is also significant for the long DM (see Figure 13(a)). Conversely, the difference between the flow front arrival time at the junction between the flow along the

top and bottom sections (see Figure 13(b)) leading to small air entrapment. Nevertheless, the total mold filling time is much shorter for the long DM than for the short DM. Thus, the length of DM should be carefully selected taking into account a compromise between the process cycle time (or mold filling time) and the part quality (or air entrapment).

5. Conclusions

We proposed the multi-layered shell element method for the numerical simulation of 3D resin flow in a laminated preform. In the multi-layered shell element method, the gapwise-averaged permeability model is not required and different permeability tensors in the thickness direction as well as the planar directions can be assigned at each layer for 3D flow simulation. Because large shell elements can be adopted, the number of nodes in the numerical mesh is significantly reduced and the computational cost saving is remarkably big compared with the conventional 3D solid element methods. The criterion for the approximate error estimation was suggested in terms of the ratio of the element size to the ply thickness and the ratio of the planar permeability to the through-thickness permeability of preform. We also proposed the criterion to quantitatively measure the computational efficiency in terms of element size. These two criteria may be helpful to optimize the element size of the multi-layered shell element method by considering both the accuracy and the efficiency. We applied this method to the numerical simulation of 3D flow for three different cases, namely impregnation of quasi-isotropic lay-up of UD plies, VARTM of boat hull and VARTM of hat-shaped stiffener, where a huge number of nodes in a numerical mesh would be required if conventional 3D solid element methods are employed. In each case, the multi-layered shell element method simulation results properly represented the particular features of 3D resin flow which cannot be obtained by the conventional 2D shell element method and the gapwise-averaged permeability model. For these examples, due to the small thickness of a single ply in the laminate, the full 3D simulation of transient flow using solid elements would need an excessively long computational time even by parallel computing. Conversely, the computational time for the multi-layered shell element method was very short, e.g. several hours, even if a single PC was used for the computation. As a consequence, this multi-layered shell element method is a very efficient and useful approach for the numerical simulation of 3D resin flow in liquid composite molding processes.

Acknowledgements

The authors acknowledge the European Union (European Regional Development Fund, FEDER) and the Hauts-de-France Region Council for co-funding the ELSAT2020 by CISIT project (POPCOM action).

References

1. Park CH. Chap 15: Numerical simulation of flow processes in composites manufacturing. In: Boisse P, editor. Advances in Composites Manufacturing and Process Design. Cambridge: Woodhead Publishing, 2015. p. 317-378.

2. Darcy H. Les fontaines publiques de la ville de Dijon. Dalmont, Paris, 1856.

3. Tari MJ, Imbert JP, Lin MY, Lavine AS, Hahn HT. Analysis of resin transfer molding with high permeability layers. J Manuf Sci Eng 1998; 120: 609-616.

4. Hsiao KT, Mathur R, Advani SG, Gillespie JW, Fink BK. A closed form solution for flow during the vacuum assisted resin transfer molding process. J Manuf Sci Eng 2000; 122: 463-475.

5. Mathur R et al. Flow front measurements and model verification in the vacuum assisted resin transfer molding process, Polym Compos 2001; 22(4): 477-490.

6. Park CH, Saouab A, Bréard J, Chatel S. A fast solution for liquid resin infusion process and simultaneous identification of distribution medium and preform permeabilities. ICCM 16. Kyoto, 8-13 July 2007.

7. Lim ST, Lee WI. An analysis of the three-dimensional resin-transfer mold filling process. Compos Sci Technol 2000; 60(7): 961-975

8. Shojaei A. Numerical simulation of three-dimensional flow and analysis of filling process in compression resin transfer moulding. Compos A 2006; 37: 1434-1450.

9. Silva L, Coupez T, Digonnet H. Massively parallel mesh adaptation and linear system solution for multiphase flows. Int J Comput Fluid Dynamics 2016; 30(6): 431-436.

10. Adams KL, Rebenfeld L. Permeability characteristics of multilayer fiber reinforcement: II. Theoretical model. Polym Comp 1991; 12: 186-190.

11. Bruschke MV, Advani SG. A finite element/control volume approach to mold filling in anisotropic porous media, Polym Comp 1990; 11: 291-304.

12. Heider D et al. Infusion design methodology for thick-section, low-permeability preforms using inter-laminar flow media. Compos A 2007; 38: 525-534.

13. Calado VMA, Advani SG. Effective average permeability of multi-layer preforms in resin transfer molding. Compos Sci Techno 1996; 56: 519-531.

14. Bancora SP, Binetruy C, Advani SG, Syerko, Comas-Cardona S. Effective permeability averaging scheme to address in-plane anisotropy effects in multi-layered preforms. Compos A 2018; 113: 359-369.

15. Kang MK, Lee WI. A dual-scale analysis of macroscopic resin flow in vacuum assisted resin transfer molding. Polym Compos 2004; 25(5): 510-520.

16. Dong C. An equivalent medium method for the vacuum-assisted resin transfer molding process simulation. J Compos Mater 2006; 40: 1193-1213.

17. Dong C. A modified rule of mixture for the vacuum-assisted resin transfer moulding process simulation. Compos Sci Technol 2008; 68: 2125-2133.

18. Sun X, Li S, Lee LJ. Mold filling analysis in vacuum-assisted resin transfer molding. Part I: SCRIMP based on a high-permeable medium. Polym Compos 1998; 19(6): 807-817.

19. Kang MK, Lee WI. A flow-front refinement technique for the numerical simulation of the resin-transfer molding process. Compos Sci Technol 1999; 59(11): 1663-1674.

20. Hirt CW, Nichols BD. Volume of fluid (VOF) method for the dynamics of free boundaries. J Comput Phys 1981; 39(1): 201-225.

21. Arbter R et al. Experimental determination of the permeability of textiles: A benchmark exercise. Compos A 2011; 42(9): 1157-1168.

22. Vernet N et al. Experimental determination of the permeability of engineering textiles: Benchmark II. Compos A 2014; 61: 172-184.

23. Agogué R, Chebil N, Deléglise-Lagardère M, Beauchêne P, Park CH. Efficient permeability measurement and numerical simulation of the resin flow in low permeability preform fabricated by automated dry fiber placement. Appl Comp Mater 2018; 25(5): 1169-1182.

24. Girardy H, Beraud JM. HiTape dry preform technology – An efficient composite automation technology for primary aircraft structures. Sampe J 2015; 51(4): 7-15.

Appendix

Video 1. Simulation result of 3D resin flow in quasi-isotropic lay-up of unidirectional plies (×100 in z)

Tables

Table 1. Material properties of the rectangular preform and DM

Material	Property	Value
DM	Permeability in x, K_{xd}	10^{-8} m^2
	Permeability in y, K_{yd}	10^{-8} m^2
	Permeability in z, K_{zd}	10^{-10} m^2
	Fiber volume fraction, $V_{f,d}$	0.2
	Thickness, h_d	0.2 mm
Preform	Permeability in x, K_{xp}	10^{-10} m^2
	Permeability in y, K_{yp}	10^{-10} m^2
	Permeability in z, K_{zp}	10^{-12} m^2
	Fiber volume fraction, $V_{f,p}$	0.5
	Thickness, h_p	0.8 mm

Table 2. Parameters for the 3D flow simulation of the rectangular preform and DM

Parameter	Case
dx/dz	1, 2, 5, 10, 20, 50, 100, 250, 375, 500
K_{xp}/K_{zp}	1, 10, 100, 1000
K_{xd}/K_{xp}	100, 1000

Table 3. Material properties of the preform and the DM for the boat hull manufacturing

Material	Property	Value
DM (Layer 1)	Permeability in x, K_{xd}	10^{-8} m^2
	Permeability in y, K_{yd}	10^{-8} m^2
	Permeability in z, K_{zd}	10^{-10} m^2
	Fiber volume fraction, $V_{f,d}$	0.2
	Thickness, h_d	0.6 mm
Preform (Layers 2 & 4)	Permeability in x, K_{xp}	0.2×10^{-10} m^2
	Permeability in y, K_{yp}	1.8×10^{-10} m^2
	Permeability in z, K_{zp}	10^{-13} m^2
	Fiber volume fraction, $V_{f,p}$	0.5
	Thickness, h_p	0.6 mm
Preform (Layer 3)	Permeability in x, K_{xp}	1.4×10^{-10} m^2
	Permeability in y, K_{yp}	0.6×10^{-10} m^2
	Permeability in z, K_{zp}	10^{-13} m^2
	Fiber volume fraction, $V_{f,p}$	0.5
	Thickness, h_p	0.6 mm

Table 4. Material properties of the preform and the DM for the hat-shaped stiffener manufacturing

Material	Property	Value
DM (Layer 1)	Permeability in x, K_{xd}	10^{-8} m^2
	Permeability in y, K_{yd}	10^{-8} m^2
	Permeability in z, K_{zd}	10^{-10} m^2
	Fiber volume fraction, $V_{f,d}$	0.2
	Thickness, h_d	0.2 mm
Preform (Layers 2 ~ 9)	Permeability in x, K_{xp}	10^{-12} m^2
	Permeability in y, K_{yp}	10^{-12} m^2
	Permeability in z, K_{zp}	10^{-15} m^2
	Fiber volume fraction, $V_{f,p}$	0.6
	Thickness, h_p	0.2 mm

Figures

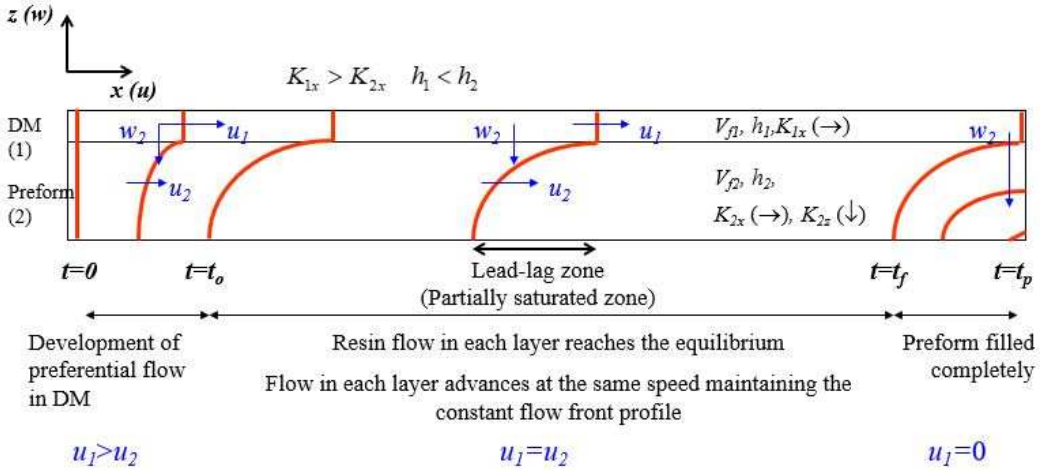

Figure 1(a)

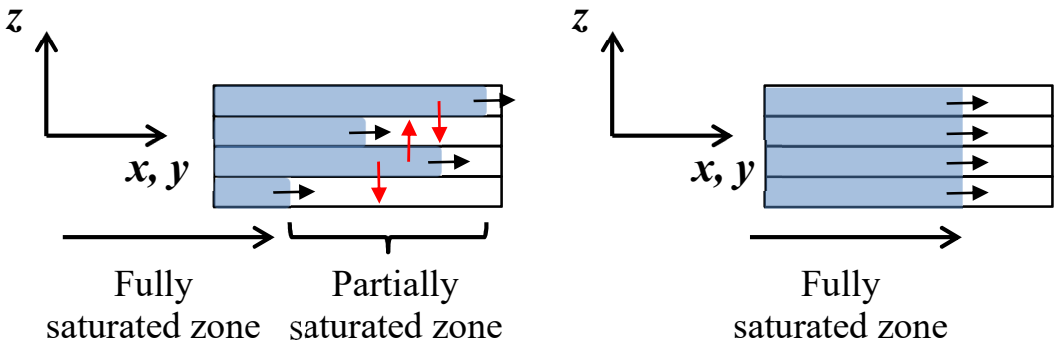

Figure 1 (b) Figure 1 (c)

Figure 1. Flow pattern in a laminated preform composed of different layers
(a) Flow pattern in the VARTM process (adapted from [6]); u_i and w_i are the flow velocity components in x and z directions respectively, $K_{i,x}$ and $K_{i,z}$ are the permeabilities in x and z directions respectively, $V_{f,i}$ is the fiber volume fraction and h_i is the layer thickness (subscript i: 1 for DM and 2 for preform)
(b) Real flow behavior in a laminated preform (with through-thickness flow in the partially saturated zone)
(c) Simplified flow behavior assumed in the gapwise-averaged permeability model (plug flow or no through-thickness flow)

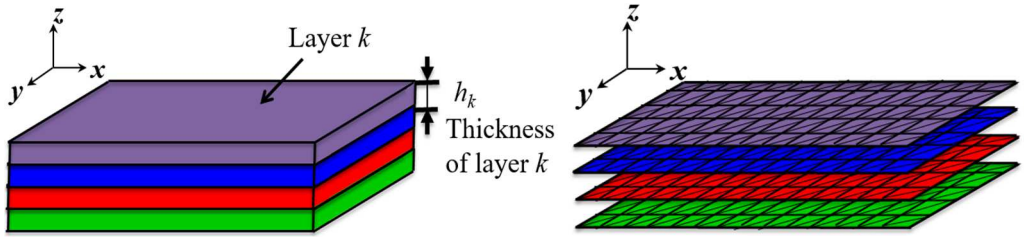

Figure 2(a) Figure 2 (b)

Figure 2. Mulyi-layered preform and multi-layered shell elements: (a) Multi-layered preform for real manufacturing process, (b) Multi-layered shell elements for numerical simulation

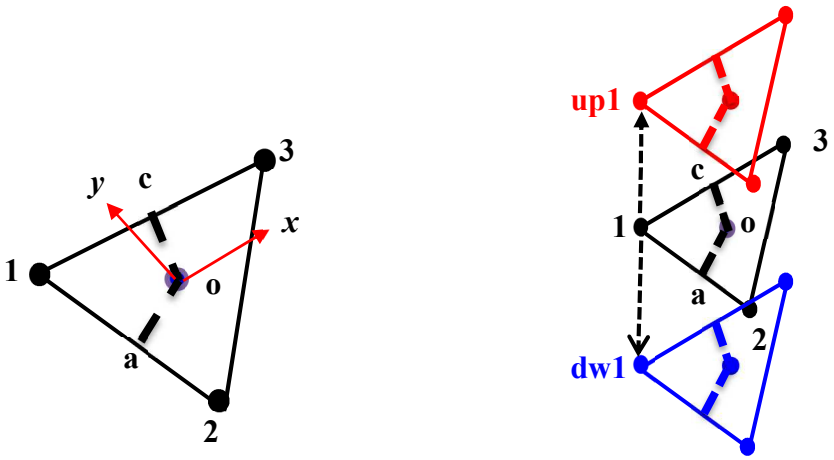

Figure 3(a) Shell element in the kth layer Figure 3(b) Upper node and bottom node of the node 1

Figure 3. Connectivity of nodes within the same layer and across the adjacent layers

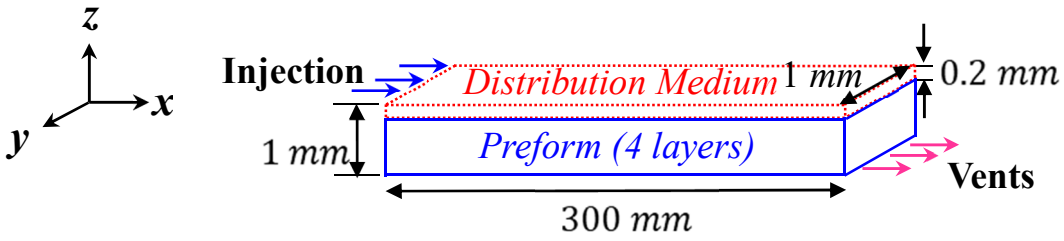

Figure 4(a) Geometry of the stack of DM and preform and injection and venting conditions

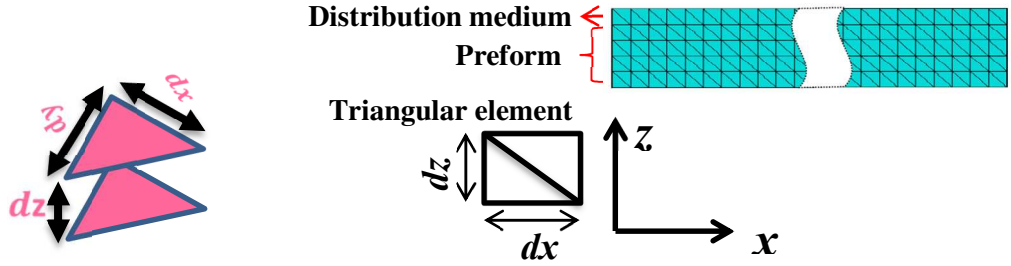

Figure 4(b) Element size definitions in multi-layered shell element (left) and in 2D shell element (right)

Figure 4. Definition of the flow condition and of the element dimensions for the 3D simulation by multi-layered shell elements and for the 2D simulation by shell elements

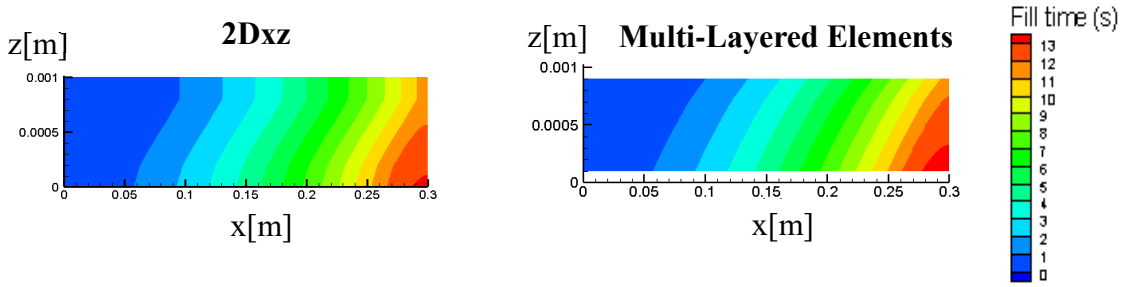

Figure 5(a) Contour of flow front arrival time in the *x*-*z* plane (magnified 100 times in *z*)

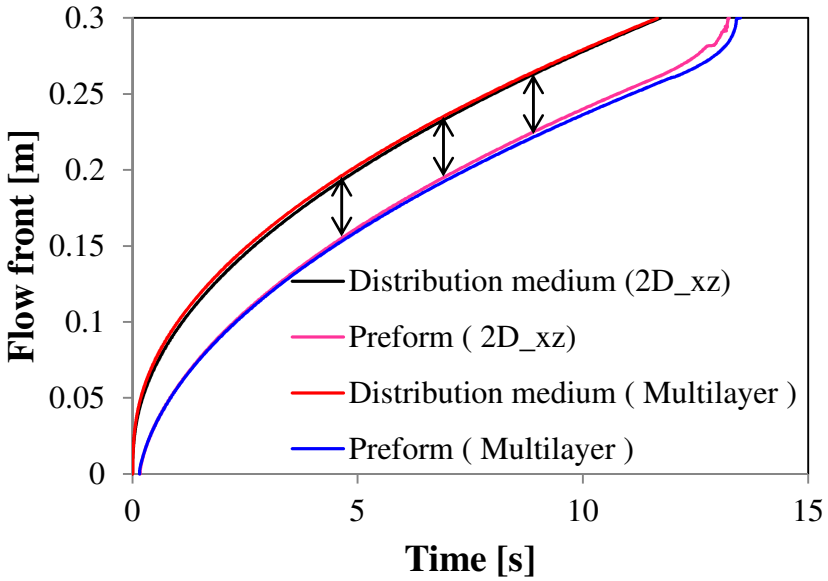

Figure 5(b) Flow front advancement at the DM and at the bottom layer of preform

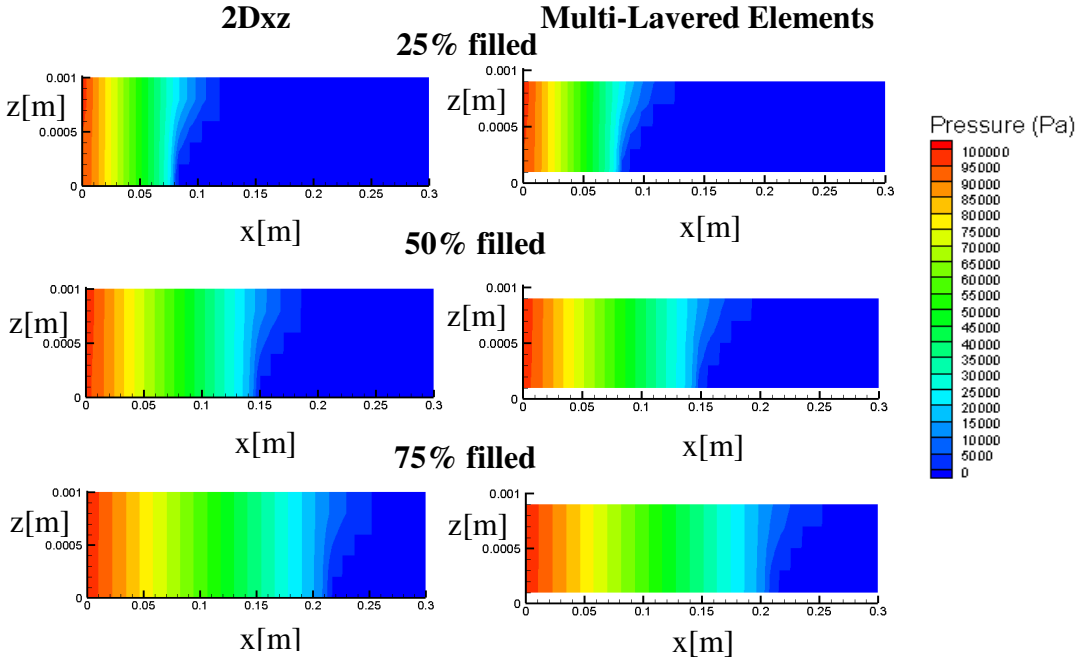

Figure 5(c) Pressure contour (magnified 100 times in z)

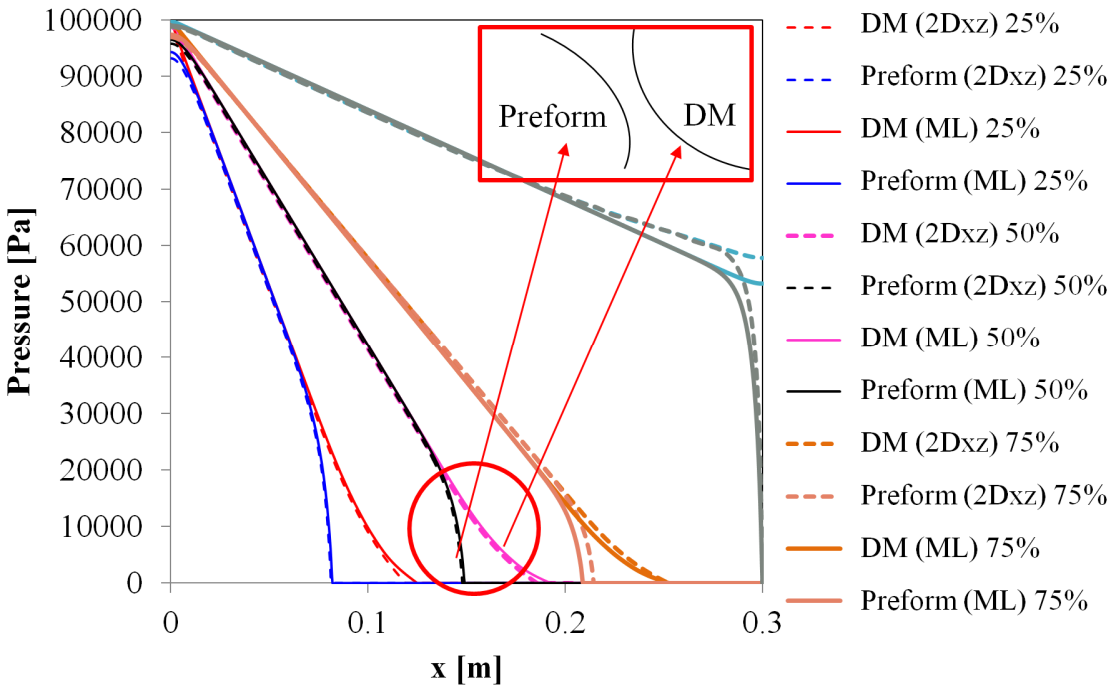

Figure 5(d) Pressure profiles at the DM and the bottom layer of preform (2Dxz: 2D simulation at the x-z plane, ML: 3D simulation by multi-layered shell elements)

Figure 5. Comparison between 2D simulation at the x-z plane and 3D simulation by multi-layered shell elements (for $dx = dy = dz$)

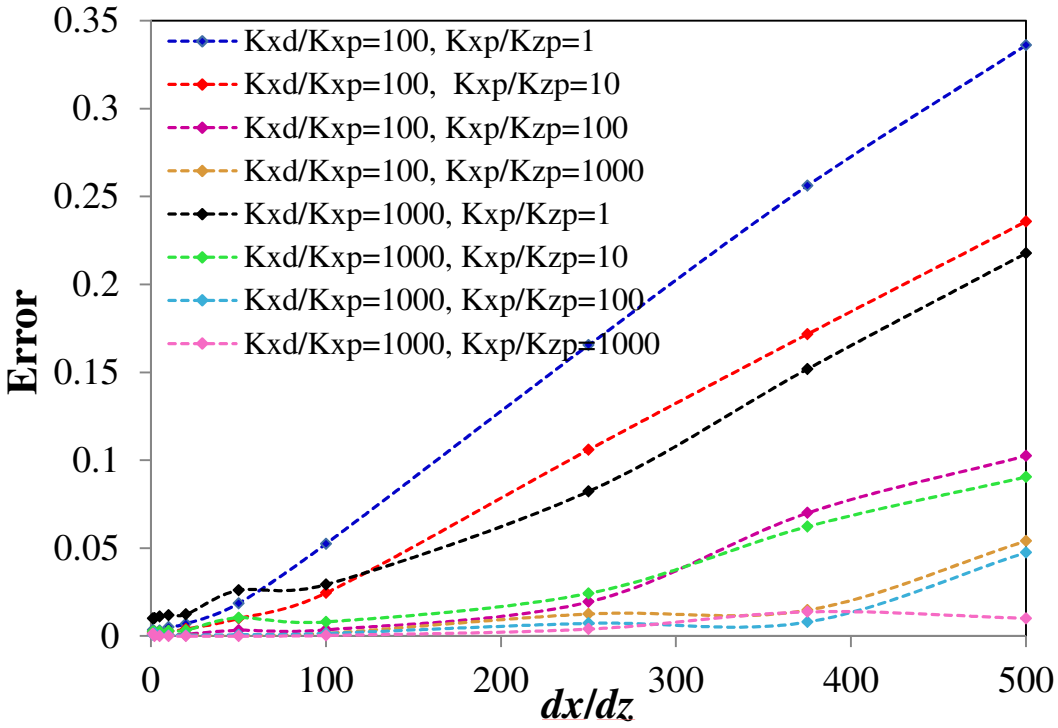

Figure 6(a) Error vs. *dx/dz*

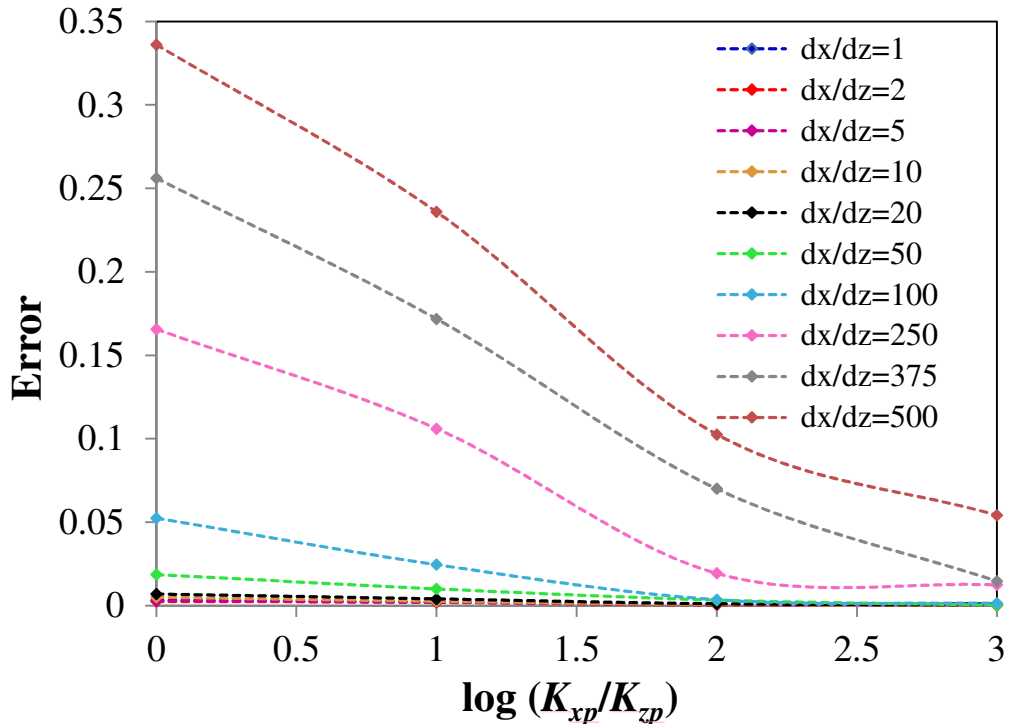

Figure 6(b) Error vs. K_{xp}/K_{zp} for different *dx/dz* (K_{xd}/K_{xp} =1000)

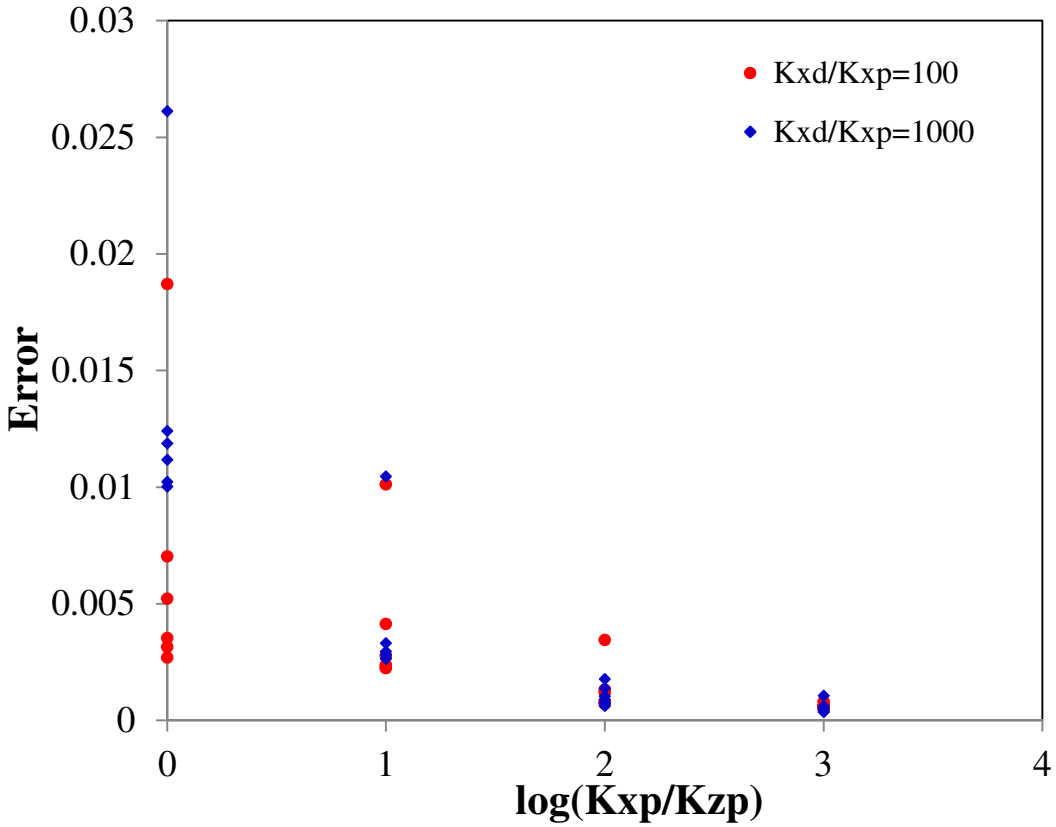

Figure 6(c) Error vs. K_{xp}/K_{zp} for different K_{xd}/K_{xp} (dx/dz = 1, 2, 5, 10, 20, 50)

Figure 6. Error in terms of element size and permeability ratios

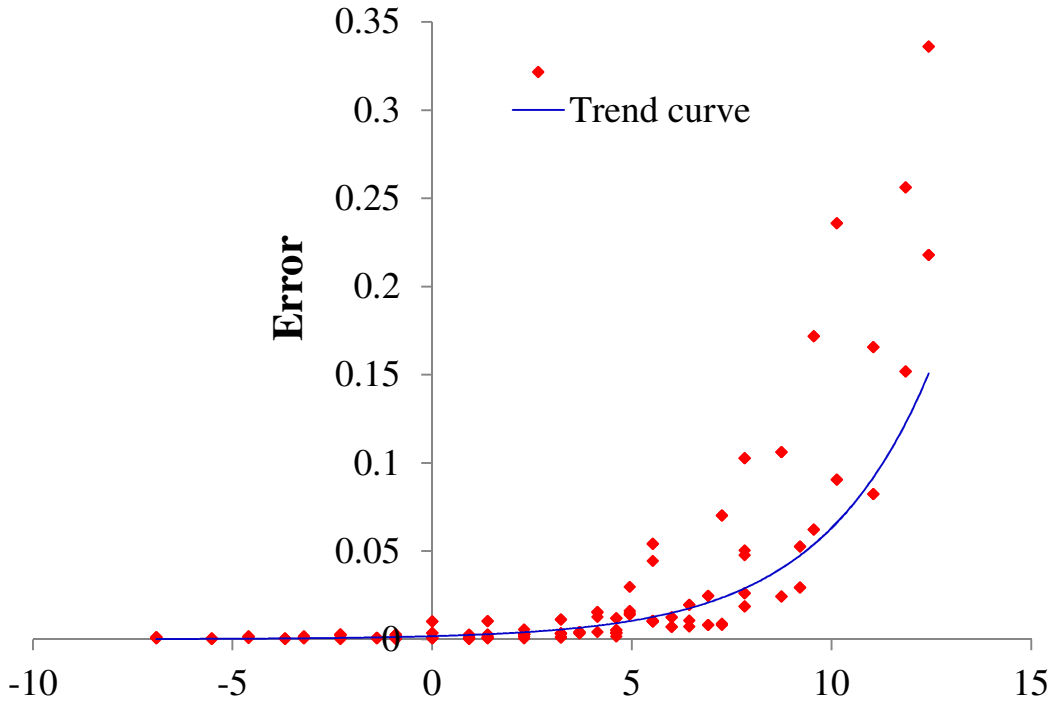

Figure 7. Error in terms of the dimensionless parameter ($\varepsilon = (dx/dz)^2(K_{zp}/K_{xp})$)

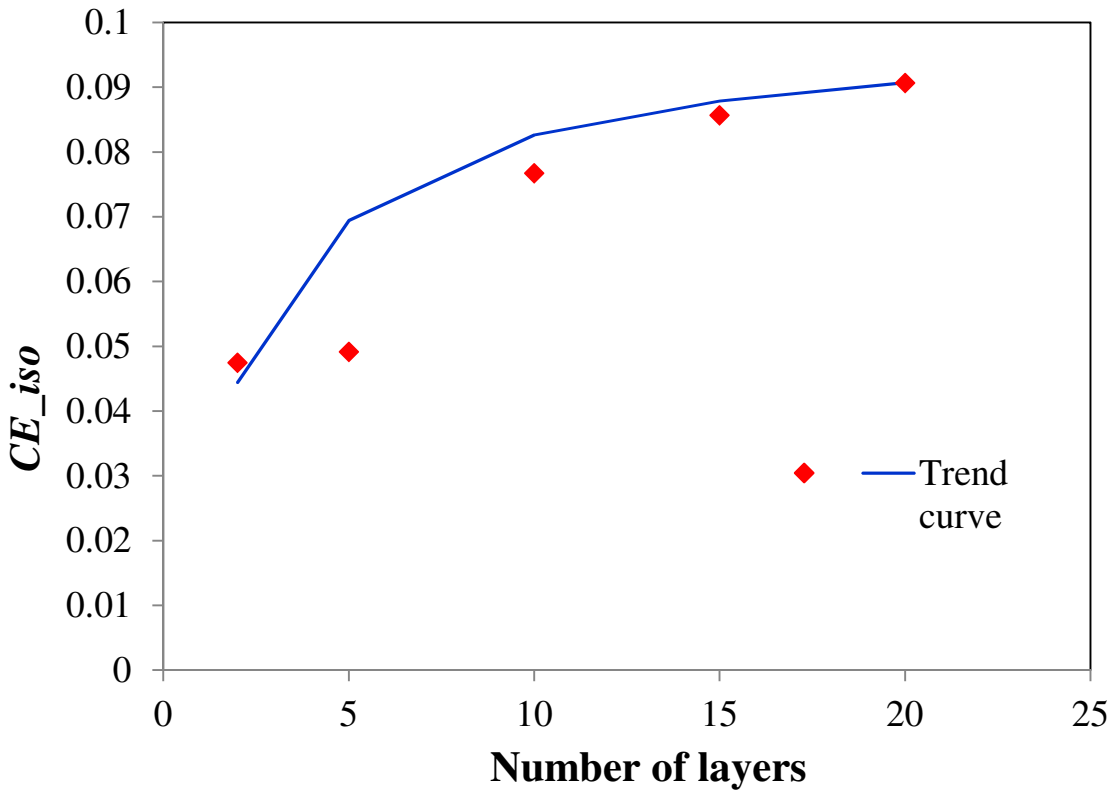

Figure 8. Coefficient of efficiency (for $dx = dy = dz$)

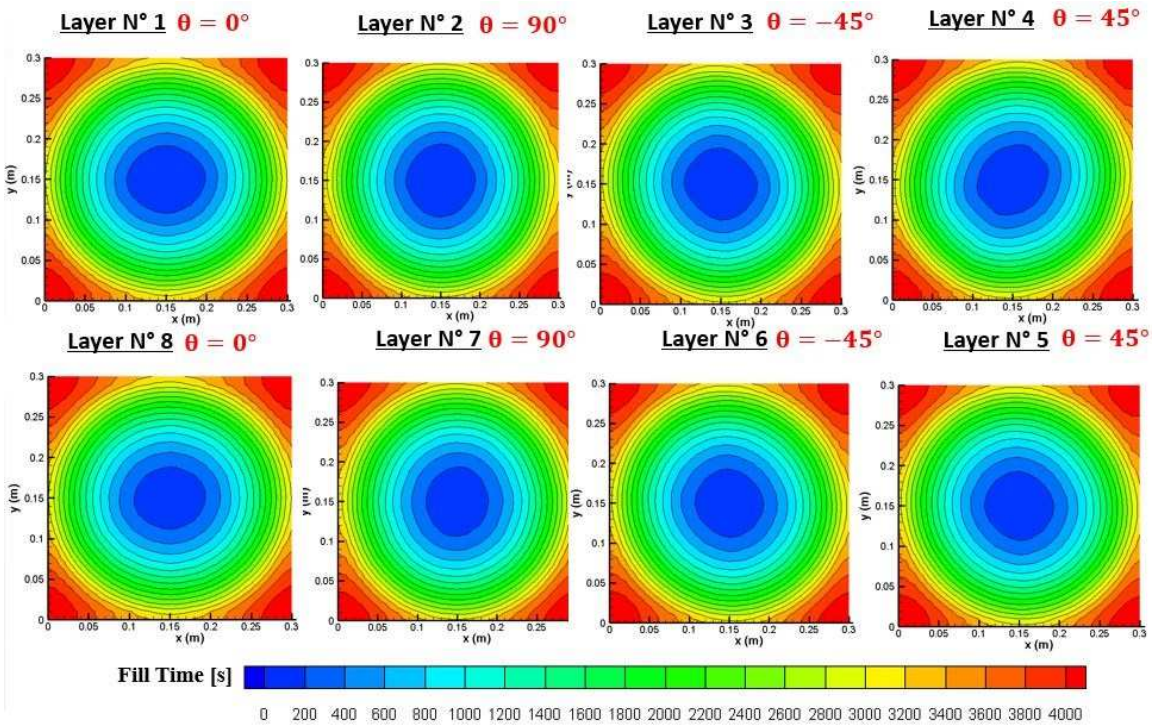

Figure 9. Flow pattern at each layer in the quasi-isotropic lay-up of UD plies ($K_2/K_3 = 100$)

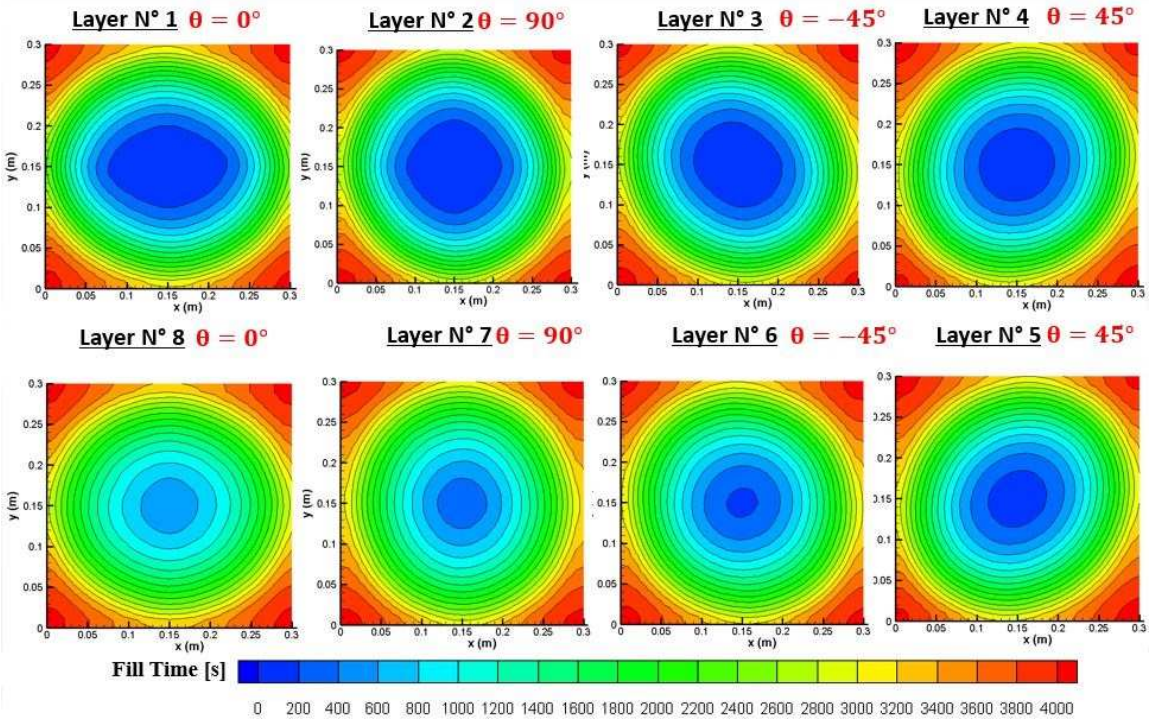

Figure 10. Flow pattern at each layer in the quasi-isotropic lay-up of UD plies (K_2/K_3 = 1000)

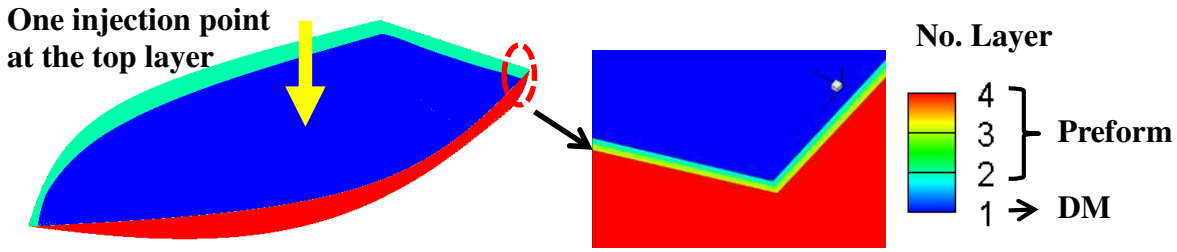

Figure 11(a) Lay-up of DM and preform for the VARTM of a boat hull

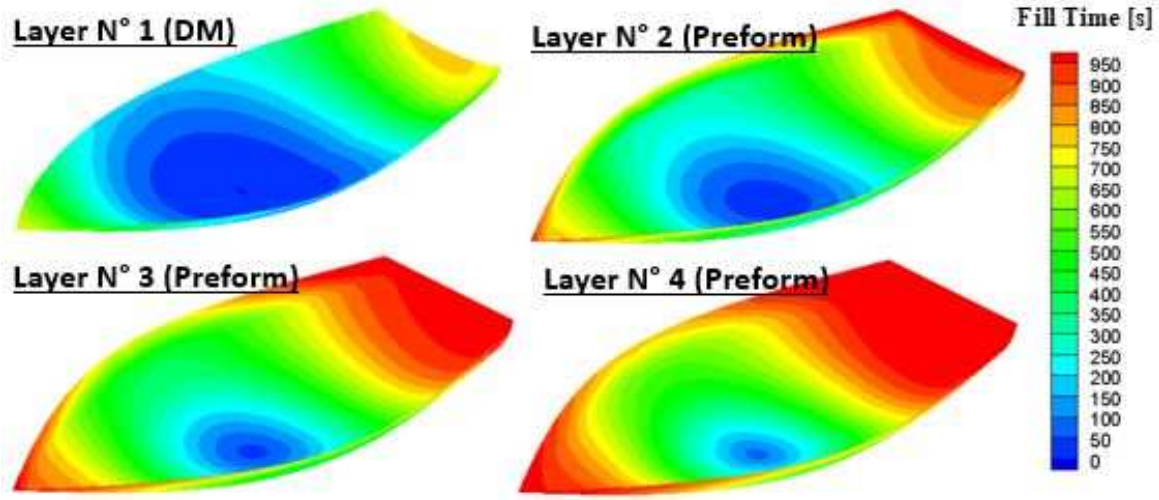

Figure 11(b) Flow pattern at each layer

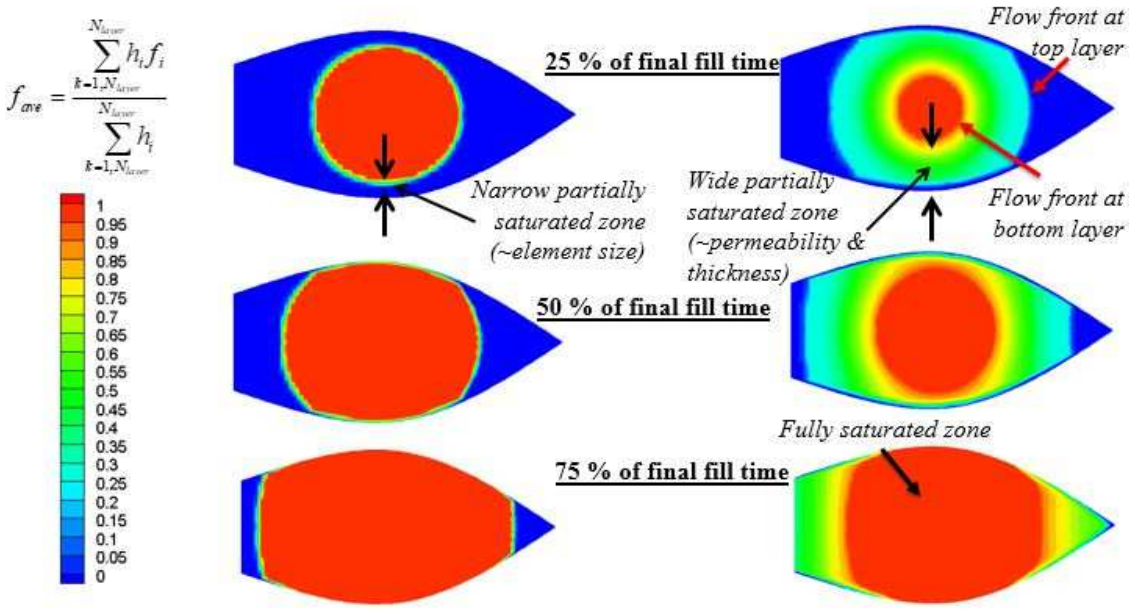

Figure 11(c) Comparison of average fill factor contour between 2D shell element method (left) and 3D multi-layered shell element method (right)

Figure 11. Results of flow simulation for the VARTM of a boat hull

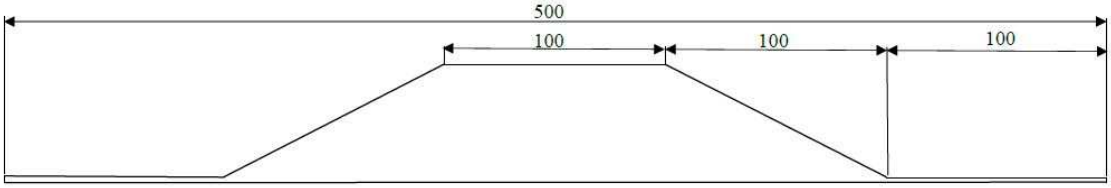

Figure 12(a) Hat-shapes stiffener shown in the *x*-*z* plane

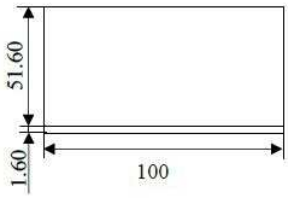

Figure 12(b) Hat-shaped stiffener shown in the *y*-*z* plane

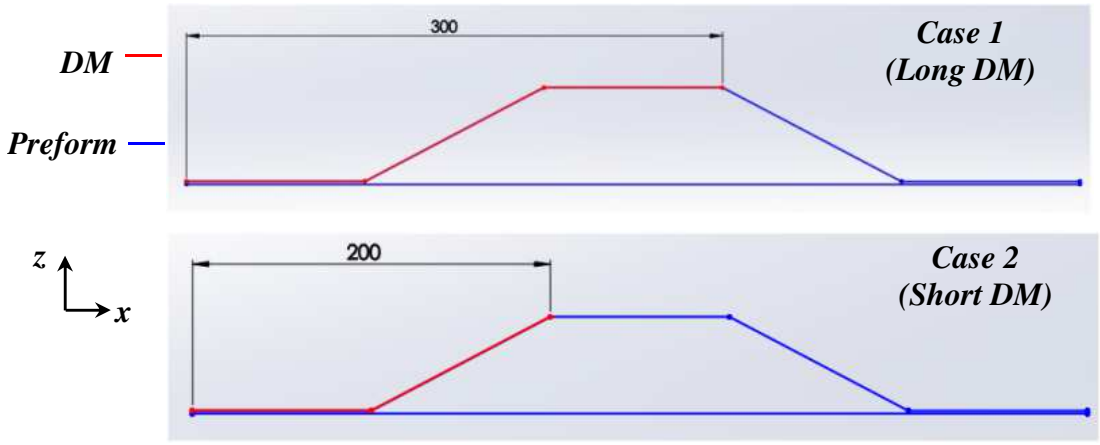

Figure 12(c) Configurations of DM (Long DM and short DM)

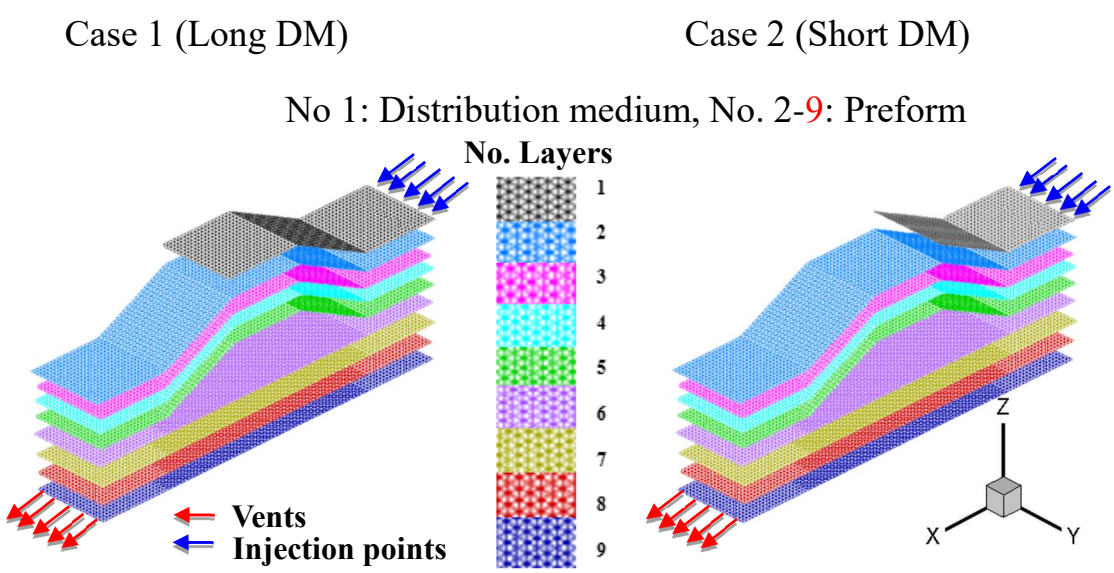

Figure 12(d) Numerical meshes and injection and venting conditions

Figure 12. Configurations of DM and geometry of hat-shaped stiffener

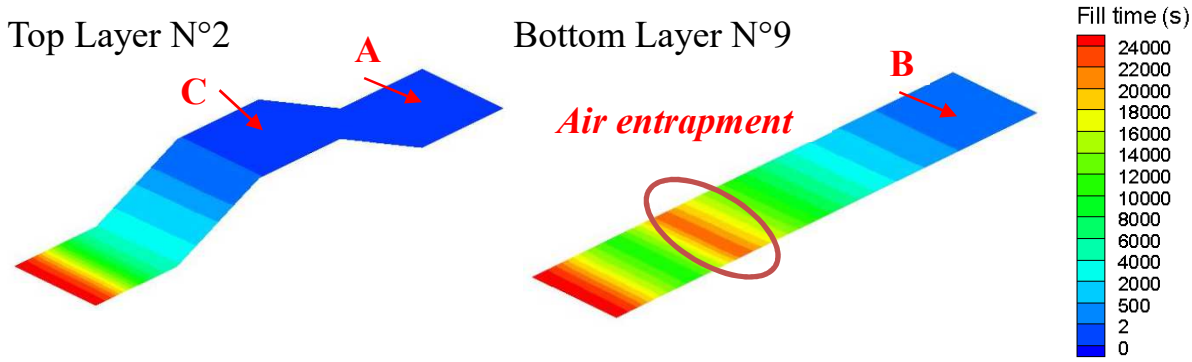

Figure 13(a) Contour of flow front arrival time for the case 1 (long DM)

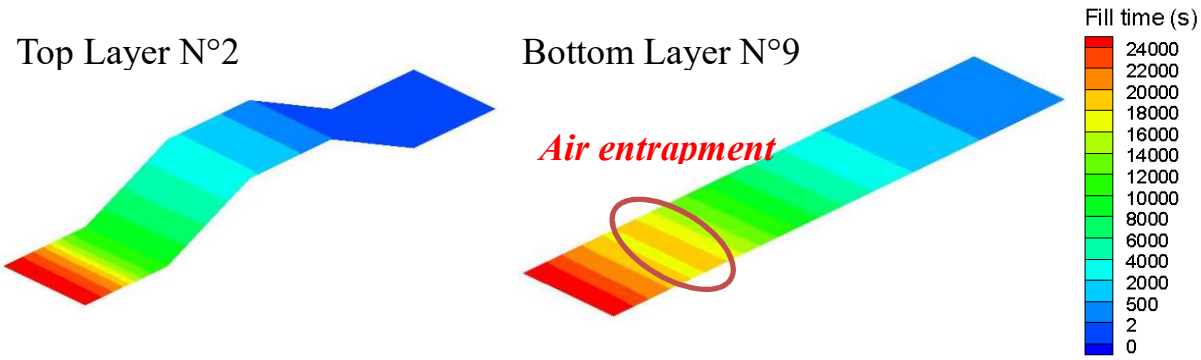

Figure 13(b) Contour of flow front arrival time for the case 2 (short DM)

Figure 13. Results of flow simulation for the hat-shaped stiffener